The Astrophysical Journal Letters, 947:L18 (8pp), 2023 April 10 https://doi.org/10.3847/2041-8213/acc940

First ALMA Maps of Cosmic-Ray Ionization Rate in High-mass Star-forming Regions

Giovanni Sabatini[1], Stefano Bovino[1,2], and Elena Redaelli[3]
[1] INAF—Istituto di Radioastronomia—Italian node of the ALMA Regional Centre (It-ARC), Via Gobetti 101, I-40129 Bologna, Italy; giovanni.sabatini@inaf.it
[2] Departamento de Astronomía, Facultad Ciencias Físicas y Matemáticas, Universidad de Concepción, Av. Esteban Iturra s/n Barrio Universitario, Casilla 160, Concepción, Chile
[3] Max-Planck-Institut für extraterrestrische Physik, Gießenbachstraße 1, D-85749 Garching bei München, Germany
Received 2023 March 6; revised 2023 March 31; accepted 2023 March 31; published 2023 April 18

Abstract

Low-energy cosmic rays (<1 TeV) are a pivotal source of ionization of the interstellar medium, where they play a central role in determining the gas chemical composition and drastically influence the formation of stars and planets. Over the past few decades, H_3^+ absorption line observations in diffuse clouds have provided reliable estimates of the cosmic-ray ionization rate relative to H_2 ($\zeta_{H_2}^{ion}$). However, in denser clouds, where stars and planets form, this method is often inefficient due to the lack of H_3^+ rotational transitions. The $\zeta_{H_2}^{ion}$ estimates are, therefore, still provisional in this context and represent one of the least understood components when it comes to defining general models of star and planet formation. In this Letter, we present the first high-resolution maps of the $\zeta_{H_2}^{ion}$ in two high-mass clumps obtained with a new analytical approach recently proposed to estimate the $\zeta_{H_2}^{ion}$ in the densest regions of molecular clouds. We obtain $\langle\zeta_{H_2}^{ion}\rangle$ that span from 3×10^{-17} to $10^{-16}\,s^{-1}$, depending on the different distribution of the main ion carriers, in excellent agreement with the most recent cosmic-ray propagation models. The cores belonging to the same parental clump show comparable $\zeta_{H_2}^{ion}$, suggesting that the ionization properties of prestellar regions are determined by global rather than local effects. These results provide important information for the chemical and physical modeling of star-forming regions.

Unified Astronomy Thesaurus concepts: Cosmic rays (329); Astrochemistry (75); Interstellar line emission (844); Star forming regions (1565); Interstellar medium (847); Massive stars (732); Star formation (1569)

1. Introduction

Cold, $T\lesssim20$ K, and dense, $n(H_2)\gtrsim10^4\,cm^{-3}$, regions within molecular clouds provide the ideal conditions for stars and planets to form. Within dense clouds, the visual extinction, A_V, becomes larger than about 3 mag so that the UV photon flux of the interstellar radiation field is attenuated. There, cosmic rays (CRs) become primary ionizing agents for the interstellar medium (ISM), also affecting the chemistry of the star-forming regions, regulating the coupling of the gas with the magnetic field (e.g., Padovani et al. 2020; Gabici 2022 as an overview).

Penetrating into molecular clouds, CRs ionize H_2 and produce several ions that are the starting point of ion–neutral chemistry. Among them, H_3^+ is directly formed by $H_2 + CR \rightarrow H_2^+ + e^-$, followed by the fast reaction $H_2^+ + H_2 \rightarrow H_3^+ + H$. Due to its simple reaction chain, H_3^+ is the pivotal molecule to quantify the CR ionization rate (CRIR) relative to molecular hydrogen (hereafter $\zeta_{H_2}^{ion}$) and to assess the role of CRs in star-forming environments (e.g., Indriolo & McCall 2012; Neufeld & Wolfire 2017; see also Luo et al. 2023a, 2023b for an alternative method recently proposed). Due to the lack of a permanent electric dipole, H_3^+, similar to H_2, does not emit rotational lines at cold temperatures. This method is hence limited to low A_V, where H_3^+ can be observed in absorption toward bright infrared (IR) sources. Furthermore, since H_3^+ is widely spread in the ISM, disentangling the contribution of other clouds on the line of sight to the source can be challenging (see, e.g., the discussion in van der Tak & van Dishoeck 2000).

Since H_3^+ is not observable, other tracers are needed to estimate $\zeta_{H_2}^{ion}$ in dense regions without strong background emission. Such methods were implemented in several works starting from the pioneering work of Black et al. (1978) where a $\zeta_{H_2}^{ion}\sim10^{-17}\,s^{-1}$ was derived based on OH, CO, and HD. Analytical approaches, based on the steady-state assumptions and the abundances of DCO^+, HCO^+, and CO, have also been explored, reporting $10^{-17}<\zeta_{H_2}^{ion}<10^{-14}\,s^{-1}$ (e.g., Caselli et al. 1998). These methods, however, depend on the number of independent tracers used to estimate the ionization fraction, i.e., $x(e)=n(e)/n(H_2)$, with $n(e)$ as the free electron density. Ivlev et al. (2019) derived a $\zeta_{H_2}^{ion}\sim10^{-16}\,s^{-1}$ with a pure theoretical method based on a self-consistent model in the prestellar core L1544.

Over the years, multiple observational techniques have been proposed to estimate $\zeta_{H_2}^{ion}$ using different molecular tracers combined with chemical models predictions: HCO^+, N_2H^+ and their isotopologues (e.g., Ceccarelli et al. 2014 and Redaelli et al. 2021b), HC_3N and HC_5N (e.g., Fontani et al. 2017), and c-C_3H_2 (e.g., Favre et al. 2018). A very promising method based on H_2 near-infrared lines has been also recently proposed by Bialy (2020) and Padovani et al. (2022). Overall, there is no consensus on $\zeta_{H_2}^{ion}$ in dense regions. The various estimates differ by orders of magnitude, representing one of the most sensitive uncertainties in astrochemical models.

In this Letter, we follow the new analytical approach proposed by Bovino et al. (2020) to estimate $\zeta_{H_2}^{ion}$ in dense molecular clouds by using ortho-H_2D^+ (hereafter o-H_2D^+) as the main observational constraint to derive the amount of H_3^+.

In the following sections, we report the details of this method and its limitations and then present our results and conclusions.

2. Methodology

The method proposed by Bovino et al. (2020) is based on the following analytical formulation:

$$\zeta_{H_2}^{ion} = k_{CO}^{o-H_3^+} \frac{X(CO)\, N(o - H_2D^+)}{3\, R_D\, \ell}, \quad (1)$$

where $k_{CO}^{o-H_3^+}$ is the rate at which CO destroys H_3^+, X(CO) is the abundance of CO relative to H_2, R_D is the deuteration of HCO^+ ($R_D = DCO^+/HCO^+$), ℓ is the path length over which the column densities (N) are estimated, and $N(o - H_2D^+)$ is the column density of the main H_3^+ isotopologue.

This methodology is shown to be accurate within a factor of 1.5–3 if the deuteration levels are well below 10% and the main H_3^+ isotopologue is H_2D^+. This means that once the latter is efficiently converted in D_2H^+ and D_3^+, the validity of the formula breaks. This method was applied to Atacama Pathfinder EXperiment (APEX) and IRAM-30 m observations in a large sample of high-mass star-forming regions, yielding $\zeta_{H_2}^{ion}$ in the range of $(0.7–6)\times10^{-17}$ s^{-1} (Sabatini et al. 2020) and has the great advantage of being model independent.

In order to apply Equation (1) at core scale, we then need to retrieve the column densities of the H_2, o-H_2D^+, DCO^+, HCO^+, and CO from high-resolution observations.

3. Source Selection and Data Reduction

The targeted sources are AGAL351.571 + 00.762 (hereafter AG351) and AGAL354.944-00.537 (hereafter AG354), which belong to the APEX Telescope Large Area Survey of the Galaxy (ATLASGAL; Schuller et al. 2009) sample, which includes $\sim10^4$ massive clumps at various evolutionary stages. Their properties are reported in Table 1. Both sources have been observed in o-$H_2D^+$with the Atacama Large Millimeter/submillimeter Array (ALMA), at a resolution of $\approx0\farcs9$ ($\sim$1400 au; at the average distance of 1.6 kpc; Redaelli et al. 2021a). Those authors analyzed the o-H_2D^+data via a dendrogram algorithm, identifying core-like structures that are believed to be truly prestellar due to the presence of o-H_2D^+emission, also reported in Figures 1(a), (b), and (c). This has also been confirmed by the absence of detected near-IR emission (Kuhn et al. 2021).

Additional ALMA observations were acquired during Cycle 8 (2021.1.00379.S; PI: G. Sabatini), using the 12-m array (Main Array) and the Atacama Compact Array (ACA), including both the 7-m array and the Total Power (TP). The 12-m array included 43–47 antennas with baselines between 15 and 500 m, while ACA 9–10 antennas, distributed over baseline ranges of 9–45 m. All the observations were carried out with a precipitable water vapor <2.5 mm.

The observations made use of the single-point mapping mode and two separate spectral setups (SeSs) with a spectral resolution $\Delta\nu = 0.1$ km s^{-1}. The first SeS covers the DCO^+ (3-2) and $C^{18}O$ (2-1) lines at $\sim$216.11 GHz and $\sim$219.56 GHz, respectively. The average angular scales covered at these frequency ranges from a resolution $\sim0\farcs7 \times 1''$ to a maximum recoverable scale of $\sim32''$, i.e., $\sim(1–50)\times10^3$ au at the average distance of 1.6 kpc. The second SeS covers the $H^{13}CO^+$ (3–2) line at $\sim$260.25 GHz (angular scales from $\sim0\farcs5$ to $\sim26''$).

Table 1
Physical and Observed Properties of the Sample

Physical Properties[a]		
	AG351	AG354
(1) R.A. (ICRS)	$17^h{:}20^m{:}51\overset{s}{.}03$	$17^h{:}35^m{:}12\overset{s}{.}03$
(2) Decl. (ICRS)	$-35^d{:}35^m{:}23\overset{s}{.}29$	$-33^d{:}30^m{:}28\overset{s}{.}97$
(3) $d_\odot$	1.3 kpc	1.9 kpc
(4) R_{GC}	7.0 kpc	7.4 kpc
(5) T_{dust}	17 K	19 K
(6) M_{gas}	170 $M_\odot$	150 $M_\odot$
Achieved Sensitivity[b] ($\langle$rms$\rangle$)		
Tracer	AG351	AG354
$(1.3\ mm)_{cont.}$	0.1 mJy beam^{-1}	0.1 mJy beam^{-1}
o-H_2D^+	300 mK	300 mK
$C^{18}O$	210 mK	220 mK
DCO^+	160 mK	160 mK
$H^{13}CO^+$	130 mK	130 mK
$^{12}C^{16}O$	80 mK	90 mK
Molecular Outflows[c]		
$^{12}C^{16}O$	no	yes

Notes.
[a] Obtained from spectra at $\Delta\nu = 0.6$ km s^{-1}. (1)–(2) ICRS phase center for ALMA pointings. (3) Heliocentric distance. (4) Galactocentric distance. (5) Dust temperature. (6) Total clump's mass.
[b] Averaged rms noise for each tracer.
[c] Possible existence of molecular outflows (see Appendix A).

All data were calibrated with the pipeline in CASA 6.2.1-7, while CASA-6.4 was employed for imaging, using the TCLEAN task. The continuum images were obtained by averaging the line-free channels in an effective bandwidth of $\sim$1.4 GHz around 224 GHz. The final beam size of the continuum maps was $\sim0\farcs7 \times 1''$. Line cubes were made assuming a briggs-robust =0.5 weighting and a multiscale option (scales: 0, 5, 15, and 50 times the pixel size). All cubes were generated with the "auto-multithresh" algorithm, with the exception of $C^{18}O$, for which we used a manual masking procedure, due to the extension of its emission. The images have 384×384 pixels with a pixel size of $0\farcs2$. Finally, the 12 and 7 m array line cubes were combined with the TP observations through the classic feathering technique. The typical 1σ rms are summarized in Table 1, while additional details are reported in Appendix A.

To correct for the absence of zero scales in the continuum maps and o-H_2D^+cubes, we used the ratio of the total flux recovered with ALMA and the one observed with the single-dish APEX, using the ATLASGAL data for the continuum and the APEX spectra in Sabatini et al. (2020) for o-H_2D^+.

4. Analysis and Results

Since the main CO and HCO^+ isotopologues are almost always optically thick (e.g., Heyer & Dame 2015), their intensity is not proportional to N. Therefore, in our analysis, we have used less abundant isotopologues (i.e., $C^{18}O$ and $H^{13}CO^+$) to obtain a much more accurate estimate of N. In this section, we summarize the procedure and the assumptions we follow to derive $\zeta_{H_2}^{ion}$.

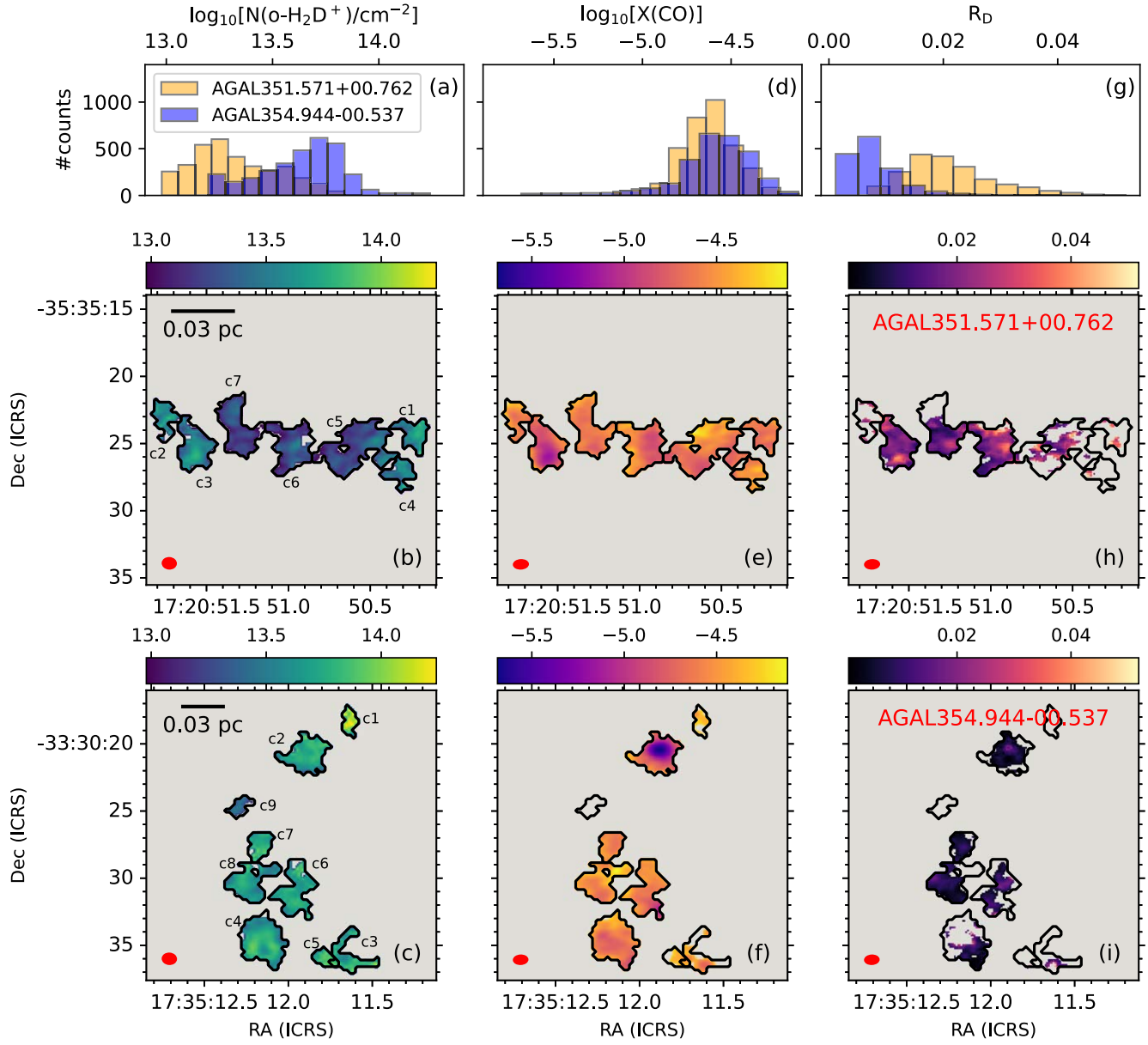

Figure 1. (a) Orange histogram (reported as a map in panel (b)) shows the number distributions of $\log_{10}[N(\text{o-H}_2\text{D}^+)/\text{cm}^{-2}]$ derived for AG351. The blue histogram is the same for AG354 (mapped in panel (c)). Panels (d), (e), and (f) are the same for $\log_{10}[\text{X(CO)}]$, while panels (g), (h), and (i) refer to R_D. Black contours in all the maps show the core structures identified in o-$\text{H}_2\text{D}^+$by Redaelli et al. (2021a). All the maps are masked with respect to the core structures. Core IDs ("c#") follow the classification defined by Redaelli et al. (2021a) and are shown as black markers in panels (b) and (c). The ALMA synthesized beams are displayed in red in the lower left corner of each map, while the scale bars are shown in the upper left corners of panels (b) and (c).

4.1. H_2 Column Density Maps

The maps of the beam-averaged H_2 column density are computed following Sabatini et al. (2022), using the dust temperature values listed in Table 1. We used a standard propagation of the uncertainties on the ALMA continuum flux, finding an average uncertainty of 8.5×10^{21} cm^{-2}. The average $N(\text{H}_2)$ values for each core span the range (1–2.5)$\times 10^{23}$ cm^{-2} and are consistent with previous measurements at 0.8 mm (Redaelli et al. 2021a).

4.2. Column Density Maps of the Molecular Tracers

The column densities of all the molecular species are estimated following Mangum & Shirley (2015), computing optical depths, τ, with Equation (5) of Caselli et al. (2008). All the molecular parameters are taken from the Cologne Database for Molecular Spectroscopy,[4] while the partition functions at the excitation temperature (T_ex) were obtained by linearly interpolating the values reported by Sabatini et al. (2020) for o-H_2D^+, Redaelli et al. (2019) for DCO^+, and the CDMS catalog for C^{18}O and H^{13}CO^+. The integral of the optical depth along the velocity axis is computed in each channel where the emission is $>3\sigma$ (see Table 1).

In order to select the T_ex value for each tracer, we analyze their different chemical properties (i.e., different critical densities, and spatial distributions). For the o-H_2D^+ we used $T_\text{ex} = 10$ K as found by Redaelli et al. (2021a). We assumed the same excitation temperature also for DCO^+ and

[4] CDMS: https://cdms.astro.uni-koeln.de/classic/.

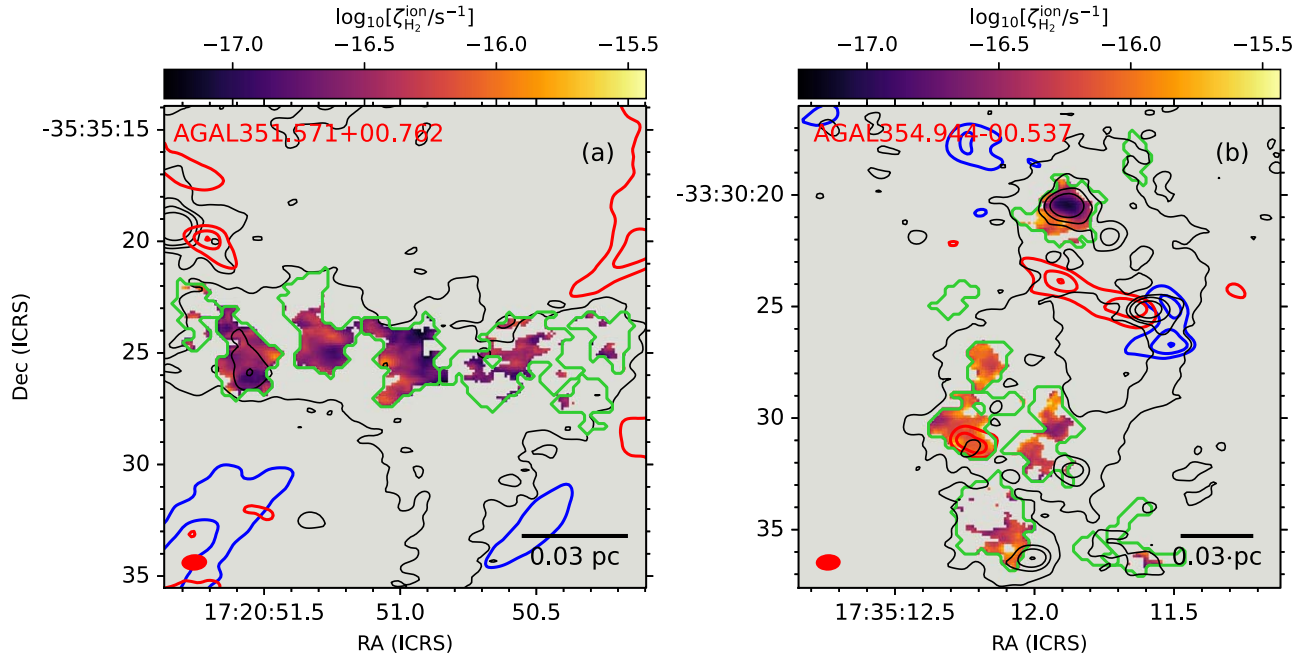

Figure 2. Map of the log $_{10}(\zeta_{H_2}^{ion})$ derived for AG351 (a) and AG354 (b). The black contours show the continuum emission at 1.33 mm (levels: [3, 6, 9, 15, 30]σ, whit $1\sigma = 0.1$ mJy beam^{-1}). The blue- and redshifted components of $^{12}C^{16}O$ emission are shown as blue and red contours, respectively, whit levels at 50%, 75%, and 99% of the peak of the CO velocity-integrated intensity. More details are given in Appendix A. Green contours mark the same core structures reported in Figure 1. The $\zeta_{H_2}^{ion}$ was derived only in those positions where all the molecular tracers have been detected at $>3\sigma$ (see Table 1). The beam size and the scale bar are shown in the bottom left and bottom right corners, respectively.

$H^{13}CO^+$ considering their chemical connection with o-H_2D^+ (e.g., Dalgarno & Lepp 1984). We note, however, that the estimate of $\zeta_{H_2}^{ion}$, obtained via Equation (1), is not directly affected by the value of $N(DCO^+)$ and $N(H^{13}CO^+)$, but rather by their ratio. Since the two species have similar molecular properties and the same transition applies to both, their abundance ratio is not strongly dependent on T_{ex}. A variation of 5 to 20 K in T_{ex} would imply a difference of $\pm 20\%$ in $N(DCO^+)/N(H^{13}CO^+)$, which is consistent with the final average error associated with the $\zeta_{H_2}^{ion}$ (see Section 4.3). The $C^{18}O$ has relatively lower critical densities ($n_c \sim 10^3$ cm^{-3}). Since we are focusing on high-density regions, it is reasonable to assume that $C^{18}O$ is thermalized by collisions with H_2 and that gas and dust are coupled (Goldsmith 2001). We hence assume $T_{ex}(C^{18}O) = T_{kin} = T_{dust}$. At these temperatures, the emission of all the tracers is mostly optically thin ($\tau < 1.1$), and the final N are consistent with those typically obtained in similar sources (e.g., Roberts et al. 2011; Morii et al. 2021; Sabatini et al. 2022).

4.3. Core-scale $\zeta_{H_2}^{ion}$ Maps

We derived X(CO) from the $C^{18}O$ abundance assuming an oxygen isotopic ratio $[^{16}O]/[^{18}O] = 58.8R_{GC} + 37.1$, where R_{GC} is the galactocentric distance of each source expressed in kpc (Wilson & Rood 1994). The resulting X(CO) span more than 1 order of magnitude, from $\sim 7 \times 10^{-6}$ to 6×10^{-5} within the individual cores (see Figures 1(d), (e), and (f)). We identify regions where the CO depletion (f_D) is almost irrelevant, with observed abundances of $C^{18}O$ as expected (see Giannetti et al. 2017), up to regions where only less than 5% of the expected CO is still present in the gas phase (i.e., $f_D > 20$). These values agree with the average f_D found by Sabatini et al. (2022) in a large sample of prestellar cores candidates embedded in young high-mass star-forming regions. For R_D, we derived $N(HCO^+)$ from $H^{13}CO^+$ assuming the ratio $[^{12}C]/[^{13}C] = 6.1R_{GC} + 14.3$ (e.g., Feng et al. 2016). The resulting R_D are in between 0.002 and 0.05 (Figures 1(g), (h), and (i)), slightly higher than those previously found by Sabatini et al. (2020) with APEX single-dish observations, and most likely due to beam-dilution effects.

In Equation (1), we employ $k_{CO}^{H_3^+} \sim 2.3 \times 10^{-9}$ cm^3 s^{-1}, which is derived at the $T_{gas} = T_{dust}$ ($\sim$18 K).[5] We highlight that a significant temperature variation (down to, e.g., $T_{gas} = 10$ K) leads to an increase of the reaction rate of less than 9%. As we account for the large-scale emission of all the tracers by including ALMA-TP in Equation (1) we have also assumed ℓ equal to the ALMA field of view.

The final $\zeta_{H_2}^{ion}$ maps are shown in Figure 2 together with the thermal continuum emission at 1.3 mm. The $\zeta_{H_2}^{ion}$ spans from $\sim 6 \times 10^{-18}$ to 2×10^{-16} s^{-1} and shows a global pattern within the cores identified in o-H_2D^+. In particular, we note that where the continuum emission is higher, the average $\zeta_{H_2}^{ion}$ tends to decrease (see Section 5). The $\zeta_{H_2}^{ion}$ estimates increase by a factor of 2 at most if we restrict our analysis to the scales covered by the interferometric data, i.e., removing the TP contribution from all tracers and taking the average core size in each source (see Appendix A) as the representative value for ℓ in Equation (1). Assuming a standard propagation of the uncertainties on the main beam temperature of each tracer observed with ALMA, the typical uncertainties on the $\zeta_{H_2}^{ion}$ estimates are in between a factor of 1.1 and 1.7.

[5] The rate is taken from the KInetic Database for Astrochemistry (KIDA), https://kida.astrochem-tools.org/, with modifications based on Sipilä et al. (2015) to take into account different isomers.

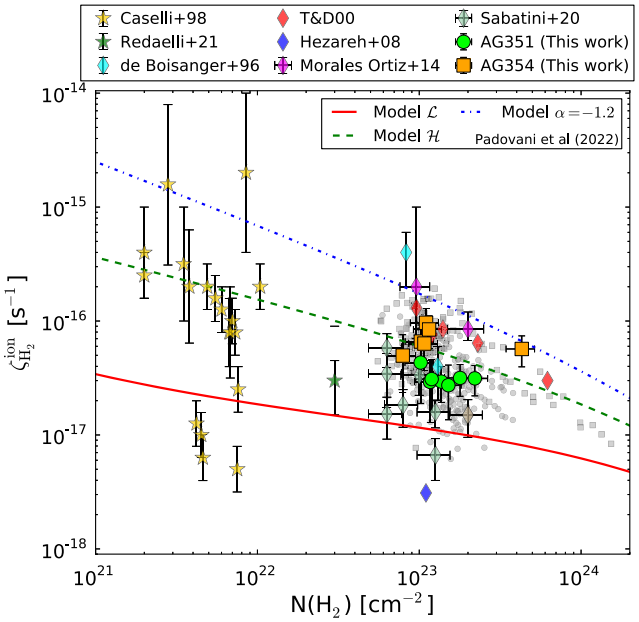

Figure 3. Estimated $\zeta_{H_2}^{ion}$ vs. $N(H_2)$ for a sample of low-mass (stars; yellow from Caselli et al. 1998, green from Redaelli et al. 2021b) and high-mass (diamonds; cyan from de Boisanger et al. 1996; red from van der Tak & van Dishoeck 2000, T&D00; see also Sabatini et al. 2020; blue from Hezareh et al. 2008; magenta from Morales Ortiz et al. 2014) star-forming regions. Gray circles and squares refer to our estimates of $\zeta_{H_2}^{ion}$ in each resolution element in Figure 2, for AG351 and AG354, respectively, while green circles and orange squares are the average values for each core identified in o-H_2D^+. The relative uncertainties on the gray circles and squares are in between 10% and 70% (Section 4.3). Dashed–dotted lines show the models discussed in Padovani et al. (2022) considering different slopes for the CR proton spectrum (see the discussion in Section 5).

5. Discussion and Conclusions

To the best of our knowledge, Figure 2 provides the first look at the $\zeta_{H_2}^{ion}$ distribution in two intermediate-mass star-forming regions observed at the remarkable angular resolution of ALMA. AG351 and AG354 are two relatively massive clumps that are similar in terms of physical properties (i.e., total clump's mass, $\langle T_{dust}\rangle$ and R_{GC}), but are far enough apart to be considered independent (Table 1). This gives us a double advantage. On the one hand, by looking at the maps in Figure 2 individually, we can assess the local variation of the $\zeta_{H_2}^{ion}$ in two separate samples of low-mass prestellar cores harbored in different parental environments (Redaelli et al. 2021a). With this approach, we reduce the impact of the initial chemical and physical conditions of the gas that originally formed the two clumps on the $\zeta_{H_2}^{ion}$. On the other hand, with two $\zeta_{H_2}^{ion}$ maps, we can also compare the $\langle\zeta_{H_2}^{ion}\rangle$ in different cores' samples, assessing the impact of the above initial conditions on the evolution, and the distribution, of $\zeta_{H_2}^{ion}$.

To better discuss the above points, we report in Figure 3 the estimates of $\zeta_{H_2}^{ion}$ obtained for a sample of high-mass (diamonds) and low-mass (stars) star-forming regions.[6] The new $\zeta_{H_2}^{ion}$ estimates obtained with ALMA are shown as gray circles (AG351) or squares (AG354). Each gray dot corresponds to a single resolution element in Figure 2 and thus has statistical significance, with typical uncertainties in between 10% and 70% (see Section 4.3). Following Sabatini et al. (2022), we have assumed a conservative error of 20% in $N(H_2)$, which corresponds to the typical uncertainty when $N(H_2)$ is derived from ALMA continuum observations. Green circles and orange squares are the $\langle\zeta_{H_2}^{ion}\rangle$ derived for the individual cores in AG351 and AG354, respectively. A comparison of the $\langle\zeta_{H_2}^{ion}\rangle$ obtained in the two sources shows that the cores belonging to the same parental clump display comparable values within the error bars. This suggests that the ionization properties are set by the global properties of the environment where the cores formed.

Our results also show a possible trend when comparing the two core populations, in that $\zeta_{H_2}^{ion}$ in AG354 appears a factor of $\approx$2 higher than in AG351. This might hint at distinct initial conditions for the two clumps or at slightly different evolutionary scenarios. Almost all prestellar cores identified in the two clumps via o-H_2D^+ have a virial parameter <1 and, unless supported by strong magnetic fields, appear to be gravitationally unstable against collapse (Kauffmann et al. 2013). As pointed out by Redaelli et al. (2021a), AG354 also reaches higher $N(H_2)$ values and degree of turbulence, with larger linewidths. As a result of the progressive accretion of material from clumps to cores, the core population in AG354 is associated with larger M_{core} and N(o-H_2D^+), while having a comparable X(o-H_2D^+) as in AG351 (see Table 2).

We have also investigated the presence of outflows in the clumps using the CO (2–1) emission (see Appendix A). We find no significant high-velocity emission in AG351, while we detect a possible bipolar outflow in AG354. This seems associated with a continuum core lacking o-H_2D^+, and it is directed in the east–west direction, without overlapping with any o-H_2D^+-identified structure. We can therefore speculate that the different $\langle\zeta_{H_2}^{ion}\rangle$ derived in AG351 and AG354 are most likely due to the different amounts of material interacting with CRs. With the available information, however, we are not able to disentangle whether the different $\zeta_{H_2}^{ion}$ that we derived in the two clumps have caused a distinct evolutionary speed or if they are on the contrary, influenced by, e.g., the presence of protostellar activity. Furthermore, it is important to highlight that the detected difference is within the accuracy of the method itself.

Figure 3 also shows the trends predicted by CR propagation models (see Padovani et al. 2018, 2022). We report three reference cases, obtained considering a single CR electron spectrum and different CR proton spectra: (i) model $\mathcal{L}$ is based on the data from the two Voyager spacecraft (e.g., Stone et al. 2019) and considers a low-energy spectral slope $\alpha=0.1$; (ii) model $\mathcal{H}$, $\alpha=-0.8$, reproduces the average value of $\zeta_{H_2}^{ion}$ in diffuse regions (see also Padovani et al. 2020; Gabici 2022); (iii) the model with $\alpha=-1.2$, which can be considered as an upper limit for the $\zeta_{H_2}^{ion}$ estimates in diffuse regions (Padovani et al. 2022). Comparing the predictions of the model with our estimates, we found a global variation of $\zeta_{H_2}^{ion}$ with $N(H_2)$, which is predicted by the CR propagation models and confirmed by observations. In both cases, the higher the $N(H_2)$ values, the lower and more concentrated the $\zeta_{H_2}^{ion}$ estimates. Our results are in remarkable agreement with the latest models of CR propagation, while the scatter of $\zeta_{H_2}^{ion}$ values derived at a given $N(H_2)$ could reflect a different morphology of magnetic fields. This effect is indeed expected from theoretical models (e.g., Padovani & Galli 2011; Padovani et al. 2013). The increasing capabilities of modern

[6] A similar plot is also provided in Appendix B, where we made a comparison with other analytical methods.

astronomical facilities, e.g., ALMA, in polarization observations will allow us in the near future to study the magnetic field properties of the targeted sources to reconstruct the complete picture of the ionization and dynamical properties of star-forming regions.

The authors thank the anonymous referee for suggestions that improved the manuscript, and gratefully acknowledge Dr. M. Padovani and Dr. D. Petry for fruitful discussions and feedback. S.B. is financially supported by ANID Fondecyt Regular (project #1220033), and the ANID BASAL projects ACE210002 and FB210003. E.R. acknowledges the support of the Max Planck Society. This publication has received support from the ORP, that is funded by the European Union's Horizon 2020 research and innovation program under grant agreement No. 101004719 (ORP). This Letter makes use of the following ALMA data: ADS/JAO.ALMA#2021.1.00379.S (PI: G. Sabatini). ALMA is a partnership of ESO (representing its member states), NSF (USA) and NINS (Japan), together with NRC (Canada), MOST and ASIAA (Taiwan), and KASI (Republic of Korea), in cooperation with the Republic of Chile. The Joint ALMA Observatory is operated by ESO, AUI/NRAO and NAOJ.

Facility: ALMA; APEX.

Software: This research has made use of APLpy (https://aplpy.readthedocs.io/en/stable/, an open-source plotting package for Python), Astropy (https://www.astropy.org/), NumPy (https://numpy.org/), Matplotlib (https://matplotlib.org/), the Cologne Database for Molecular Spectroscopy (CDMS, https://cdms.astro.uni-koeln.de/), the KInetic Database for Astrochemistry (KIDA, https://kida.astrochem-tools.org/), and the NASA Astrophysics Data System Bibliographic Services (ADS, https://ui.adsabs.harvard.edu/).

Appendix A
Core Properties and Molecular Outflow Identification

This appendix summarizes the physical properties derived for the core populations that are harbored in AG351 and AG354. In Table 2 we report the average values of several physical and chemical quantities of the cores. For some of them—e.g., the effective radius ($R_{\rm eff}$), and the virial and total gas masses ($M_{\rm vir}$ and $M_{\rm core}$, respectively)—we refer to Redaelli et al. (2021a) for a comprehensive description of their derivation. All the other quantities were obtained by averaging the value shown, or used to derive the parameters, in Figures 1 and 2.

As an additional view on the dynamical state of the gas globally involved in the clumps, we have investigated the presence of protostellar molecular outflows using the CO (2–1) emission. The CO data are part of the ALMA campaign described in Section 3. We observed the $^{12}C^{16}O$ (2–1) line at ∼230.54 GHz in a third SeS centered at 230.5 GHz. The data were taken with a spectral resolution of 0.6 km s^{-1}, which is 6 times larger than that of the other tracers, to maximize the sensitivity and provide a good detection of the thermal continuum emission. The calibration and the imaging were performed in accordance with Section 3. Figure 2 shows the blue- and redshifted components (blue and red contours, respectively) of the CO emission (12m+7m+TP), superimposed on the $\zeta_{\rm H_2}^{\rm ion}$ maps. The blue- and redshifted components were derived by integrating the CO emission in the velocity ranges between ∼[−20, −6] km s^{-1} and ∼[−2, 35] km s^{-1}, respectively. The presence of protostellar molecular outflows seems evident only in core-2 of AG354 (see Figure 2 and Table 2). In this case, the outflow has a projected size of a few arcseconds, but it never overlaps with any of the structures where the column densities and $\zeta_{\rm H_2}^{\rm ion}$ were derived. On the contrary, AG351 lacks any evidence of protostellar activity.

Table 2
Physical Properties of the Cores Harbored in AG351 and AG354

Core ID[a]	$R_{\rm eff}$[a] (au)	$M_{\rm vir}$[a] ($M_\odot$)	$M_{\rm core}$[a] ($M_\odot$)	$N(H_2)$ ($\times10^{23}$ cm^{-2})	N(o-H_2D^+) ($\times10^{13}$ cm^{-2})	$R_{\rm D}$ ($\times10^{-2}$)	$R_{\rm H}$ ($\times10^{-5}$)	X(CO) ($\times10^{-5}$)	$f_{\rm D}$	$\zeta_{\rm H_2}^{\rm ion}$ ($\times10^{-17}$ s^{-1})
(AG351) c1	1500	0.4 ± 0.1	0.7 ± 0.2	1.5 ± 0.3	3.8 ± 0.9	3.4 ± 1.6	0.3 ± 0.1	2.3	5.4	2.7 ± 1.4
(AG351) c2	1400	0.7 ± 0.3	0.5 ± 0.2	1.0 ± 0.2	3.3 ± 0.8	2.7 ± 1.4	0.4 ± 0.1	3.0	4.4	4.3 ± 2.4
(AG351) c3	2700	1.0 ± 0.4	1.8 ± 0.6	2.2 ± 0.4	3.2 ± 0.6	2.1 ± 0.6	0.7 ± 0.1	1.6	8.8	3.1 ± 0.9
(AG351) c4	1400	0.4 ± 0.2	0.4 ± 0.1	1.2 ± 0.2	3.0 ± 0.9	3.4 ± 1.8	0.3 ± 0.1	2.8	4.3	2.9 ± 1.6
(AG351) c5	2700	0.6 ± 0.1	1.6 ± 0.5	1.2 ± 0.2	1.9 ± 0.2	2.3 ± 1.1	0.4 ± 0.1	2.8	4.8	3.1 ± 1.5
(AG351) c6	2100	1.1 ± 0.3	1.1 ± 0.4	1.4 ± 0.3	1.8 ± 0.2	2.2 ± 0.7	0.6 ± 0.1	2.4	5.8	2.9 ± 1.0
(AG351) c7	2200	0.5 ± 0.1	1.6 ± 0.5	1.8 ± 0.4	1.7 ± 0.2	1.6 ± 0.4	0.6 ± 0.1	2.3	5.3	3.2 ± 1.0
(AG354) c2	2900	0.8 ± 0.2	5.6 ± 1.8	4.3 ± 0.9	5.0 ± 0.8	0.7 ± 0.1	3.3 ± 0.5	1.1	16.8	5.7 ± 1.7
(AG354) c3	2300	0.7 ± 0.3	1.1 ± 0.4	0.8 ± 0.2	5.1 ± 1.2	2.1 ± 1.0	0.7 ± 0.2	2.9	4.3	5.0 ± 2.6
(AG354) c4	3300	1.6 ± 0.5	3.0 ± 1.0	1.1 ± 0.2	4.9 ± 0.7	1.3 ± 0.6	1.3 ± 0.4	2.3	5.3	6.3 ± 2.6
(AG354) c6	2900	2.0 ± 0.4	2.2 ± 0.7	1.0 ± 0.2	4.8 ± 0.4	1.5 ± 0.5	0.8 ± 0.2	2.6	4.6	6.6 ± 2.6
(AG354) c7	1900	1.5 ± 1.3	1.2 ± 1.2	1.1 ± 0.2	5.4 ± 0.6	1.0 ± 0.3	0.9 ± 0.3	2.8	4.2	9.6 ± 3.3
(AG354) c8	2800	1.1 ± 0.2	2.1 ± 0.7	1.2 ± 0.2	4.2 ± 0.3	1.1 ± 0.3	1.0 ± 0.2	3.1	3.9	8.4 ± 2.7

Note.
[a] IDs and values taken from Redaelli et al. (2021a); see also Figure 1. For the sake of clarity, the Table only summarizes the average properties of the cores for which $\zeta_{\rm H_2}^{\rm ion}$ is available. From left to right: effective radius; virial mass; total gas mass; average column density of H_2; average o-H_2D^+ column density; deuterium fraction, $N(DCO^+)/N(HCO^+)$; hydrogenation fraction, $N(HCO^+)/N(CO)$; CO/H_2 abundance from $C^{18}O$, with a typical uncertainty of $\lesssim$10% derived considering the average error in the $R_{\rm GC}$ of each source (see Urquhart et al. 2018); CO-depletion factor (typical uncertainty of ∼15%; see Sabatini et al. 2022); average $\zeta_{\rm H_2}^{\rm ion}$ as derived in Section 4.3.

Appendix B
Comparison with Previous Methods

In this appendix, we provide results obtained with the analytical method proposed by Caselli et al. (1998). We note that already in Caselli et al. (1998), the authors avoided the use of this method and preferred to run chemical models to estimate the $\zeta_{H_2}^{ion}$ in several low-mass cores. The limitations of this formulation are also discussed in Caselli et al. (2002) and lie primarily in the lack of some terms in the chemistry of H_2D^+ and the reactions involving electrons, and it appears to greatly overestimate $x(e)$ and the associated $\zeta_{H_2}^{ion}$. However, recent studies have used this method to estimate the $\zeta_{H_2}^{ion}$ in a protostellar source (Cabedo et al. 2023), where the physical conditions are far from the range of applicability of the original formula (determined at 10 K and for early stages of star-forming regions). For the Bok Globule B335, which hosts a Class-0 protostar with already developed outflow, Cabedo et al. (2023) obtained a $\zeta_{H_2}^{ion} \sim 7 \times 10^{-14}$ s^{-1}, by assuming a $T_{ex} = 25$ K for each species. They explain the resulting $\zeta_{H_2}^{ion}$ as a local effect of the protostellar activity, which, however, would also affect f_D that will decrease at $T_{gas} > 20$ K, when CO is efficiently desorbed in the gas phase. However, their resulting f_D present values of about 80 at the position of the protostellar embryo, i.e., an unexpected extremely high depleted region. It is also worth noting that any other process that might affect the estimates of f_D (such as the UV photodissociation of CO due to protostellar activity or the CO conversion to other species such as HCO^+ by CRs) would prevent the application of the method proposed by Caselli et al. (1998), since the underlying assumptions imply that only a fraction of C and O (i.e., $1/f_D$) remains in the gas phase, while the rest is frozen, in the form of CO, on the surface of the grains. To understand the results reported by Cabedo et al. (2023), we then decided to apply the formula proposed by Caselli et al. (1998) to our sources, which fall in the correct range of applicability being prestellar in nature. From the comparison between a prestellar and a protostellar source we can then inspect the validity of the method and its reliability.

Figure 4 summarizes the results of this test: Panel (a) shows the f_D distributions derived from $C^{18}O$, assuming a canonical CO abundance that varies with R_{GC} and the $[^{16}O]/[^{18}O]$ ratio in Section 4.3. The CO-depletion factors derived in this way always verify the condition of applicability for Caselli et al. (1998), which requires $R_D < 0.023 \times f_D$. Panel (b) shows the $x(e)$ obtained from Equation (3) in Caselli et al. (1998). Panel (c) shows the hydrogenation fraction (R_H) from the HCO^+/CO ratio. We stress that the ranges of f_D and R_H reported in Figure 4 are consistent with what is typically reported in the literature for similar sources (e.g., Caselli et al. 1998; Sabatini et al. 2022), while we find $x(e)$ a factor of 10–100 larger (see de Boisanger et al. 1996; Caselli 2002). Panel (d) shows the comparison between the $\zeta_{H_2}^{ion}$ obtained following Bovino et al. (2020; squares) and Caselli et al. (1998; stars). The latter span values in between 10^{-16} and 10^{-13} s^{-1}, i.e., from 1 to 2 orders of magnitude larger than the ones obtained with the method of Bovino et al. (2020). In addition, they tend to overestimate the upper limits provided by the CR propagation model with

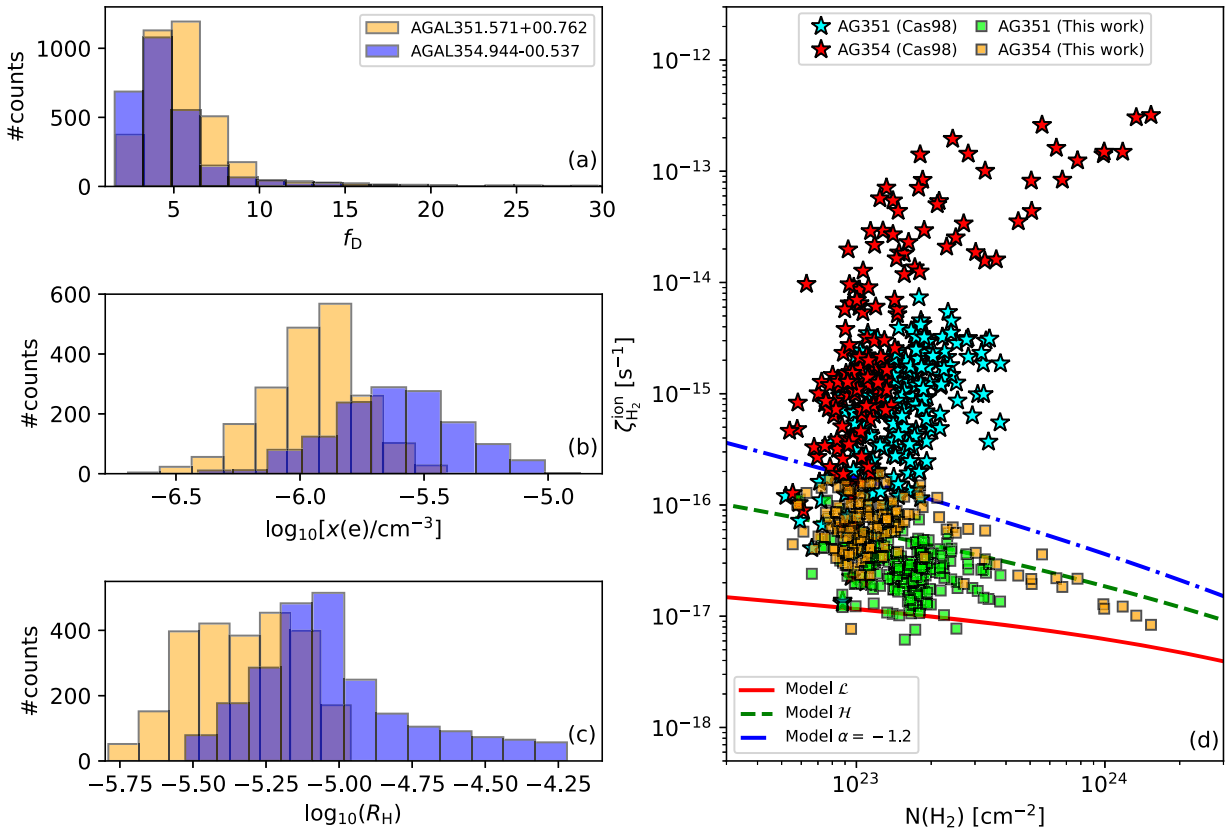

Figure 4. Panels (a), (b), and (c) show the number distributions of f_D, $x(e)$, and R_H, respectively (orange for AG351 and blue for AG354). Panel (d) compares the $\zeta_{H_2}^{ion}$ derived using the method of Caselli et al. (1998; stars) or Bovino et al. (2020; squares) as a function of $N(H_2)$. Colors refer to different sources, while the line profiles are the same models discussed in Figure 3.

$\alpha = -1.2$. This discrepancy also increases when moving to larger $N(H_2)$.

All the values reported in Figures 4(a), (b), and (c) are similar to those obtained by Cabedo et al. (2023), even if the analyzed samples show very different physical conditions. From this result, we conclude that the method proposed by Caselli et al. (1998) shows significant limitations in its applicability. For a more in-depth discussion of the limits of the methods, we refer to Caselli et al. (2002).

ORCID iDs

Giovanni Sabatini https://orcid.org/0000-0002-6428-9806
Stefano Bovino https://orcid.org/0000-0003-2814-6688
Elena Redaelli https://orcid.org/0000-0002-0528-8125

References

Bialy, S. 2020, CmPhy, 3, 32
Black, J. H., Hartquist, T. W., & Dalgarno, A. 1978, ApJ, 224, 448
Bovino, S., Ferrada-Chamorro, S., Lupi, A., Schleicher, D. R. G., & Caselli, P. 2020, MNRAS: Letters, 495, L7
Cabedo, V., Maury, A., Girart, J. M., et al. 2023, A&A, 669, A90
Caselli, P. 2002, P&SS, 50, 1133
Caselli, P., Vastel, C., Ceccarelli, C., et al. 2008, A&A, 492, 703
Caselli, P., Walmsley, C. M., Terzieva, R., & Herbst, E. 1998, ApJ, 499, 234
Caselli, P., Walmsley, C. M., Zucconi, A., et al. 2002, ApJ, 565, 344
Ceccarelli, C., Dominik, C., López-Sepulcre, A., et al. 2014, ApJL, 790, L1
Dalgarno, A., & Lepp, S. 1984, ApJL, 287, L47
de Boisanger, C., Helmich, F. P., & van Dishoeck, E. F. 1996, A&A, 310, 315
Favre, C., Ceccarelli, C., López-Sepulcre, A., et al. 2018, ApJ, 859, 136
Feng, S., Beuther, H., Zhang, Q., et al. 2016, A&A, 592, A21
Fontani, F., Ceccarelli, C., Favre, C., et al. 2017, A&A, 605, A57
Gabici, S. 2022, A&ARv, 30, 4
Giannetti, A., Leurini, S., Wyrowski, F., et al. 2017, A&A, 603, A33
Goldsmith, P. F. 2001, ApJ, 557, 736
Heyer, M., & Dame, T. M. 2015, ARA&A, 53, 583
Hezareh, T., Houde, M., McCoey, C., Vastel, C., & Peng, R. 2008, ApJ, 684, 1221
Indriolo, N., & McCall, B. J. 2012, ApJ, 745, 91
Ivlev, A. V., Silsbee, K., Sipilä, O., & Caselli, P. 2019, ApJ, 884, 176
Kauffmann, J., Pillai, T., & Goldsmith, P. F. 2013, ApJ, 779, 185
Kuhn, M. A., de Souza, R. S., Krone-Martins, A., et al. 2021, ApJS, 254, 33
Luo, G., Zhang, Z.-Y., Bisbas, T. G., et al. 2023a, ApJ, 942, 101
Luo, G., Zhang, Z., Bisbas, T. G., et al. 2023b, ApJ., 946, 91
Mangum, J. G., & Shirley, Y. L. 2015, PASP, 127, 266
Morales Ortiz, J. L., Ceccarelli, C., Lis, D. C., et al. 2014, A&A, 563, A127
Morii, K., Sanhueza, P., Nakamura, F., et al. 2021, ApJ, 923, 147
Neufeld, D. A., & Wolfire, M. G. 2017, ApJ, 845, 163
Padovani, M., Bialy, S., Galli, D., et al. 2022, A&A, 658, A189
Padovani, M., & Galli, D. 2011, A&A, 530, A109
Padovani, M., Hennebelle, P., & Galli, D. 2013, A&A, 560, A114
Padovani, M., Ivlev, A. V., Galli, D., et al. 2020, SSRv, 216, 29
Padovani, M., Ivlev, A. V., Galli, D., & Caselli, P. 2018, A&A, 614, A111
Redaelli, E., Bizzocchi, L., Caselli, P., et al. 2019, A&A, 629, A15
Redaelli, E., Bovino, S., Giannetti, A., et al. 2021a, A&A, 650, A202
Redaelli, E., Sipilä, O., Padovani, M., et al. 2021b, A&A, 656, A109
Roberts, H., van der Tak, F. F. S., Fuller, G. A., Plume, R., & Bayet, E. 2011, A&A, 525, A107
Sabatini, G., Bovino, S., Giannetti, A., et al. 2020, A&A, 644, A34
Sabatini, G., Bovino, S., Sanhueza, P., et al. 2022, ApJ, 936, 80
Schuller, F., Menten, K. M., Contreras, Y., et al. 2009, A&A, 504, 415
Sipilä, O., Caselli, P., & Harju, J. 2015, A&A, 578, A55
Stone, E. C., Cummings, A. C., Heikkila, B. C., & Lal, N. 2019, NatAs, 3, 1013
Urquhart, J. S., König, C., Giannetti, A., et al. 2018, MNRAS, 473, 1059
van der Tak, F. F. S., & van Dishoeck, E. F. 2000, A&A, 358, L79
Wilson, T. L., & Rood, R. 1994, ARA&A, 32, 191